IMAGE-BASED SCREENING METHODS FOR REDUCING MISDIAGNOSIS OF CARPOMETACARPAL FRACTURE AND DISLOCATION

By

KAICHENG WU

A thesis submitted to the

School of Graduate Studies

Rutgers, The State University of New Jersey

In partial fulfillment of the requirements

For the degree of

Master of Science

Graduate Program in Industrial And Systems Engineering

Written under the direction of

Dr. Kang Li

And approved by

_____

_____

_____

New Brunswick, New Jersey

October, 2018

ABSTRACT OF THE THESIS

Image-based Screening Methods For Reducing Misdiagnosis Of Carpometacarpal Fracture And Dislocation

By KAICHENG WU

Thesis Director:

Dr. Kang Li

Ulnar-sided carpometacarpal joint dislocation has been commonly missed on initial examination. The traditional diagnosis procedure manually determines the injuries based on the angles between the index metacarpal and the fourth or fifth metacarpal on the posteroanterior or lateral radiographs. This procedure is limited since metacarpal bones are difficult to identify due to osseous overlaps. This thesis develops an image-based screening method for reducing misdiagnosis of ulnar-sided carpometacarpal (CMC) fracture and dislocation.

The screening method uses a computer-aided computational framework to calculate our proposed angles for diagnosing purpose. Each step in the computaional framework is strictly defined to ensure high re-producibility and inter- and intra- observer reliability. We develop two similar frameworks for calculating 2D and 3D angles, while 3D version is only for comparison purpose.

We propose the two sets of capiate-based angles for diagnosis purpose: 1) the angle from lateral view; 2) the surrogate spatial angle calculated from lateral view angle and posteroanterior (PA) view angle: $\hat{\theta} = \sqrt{\theta_{\text{lateral}}^2 + \theta_{\text{PA}}^2}$. We show that by using the computational framework to calculate our proposed angles, the sreening method can effectively

diagnose ulnar-sided CMC fracture and dislocation. Moreover, compared to traditional method, it can reduce the confusion associated with carpometacarpal injuries and have better sensitivity and specificity. Notably, the surrogate spatial angle further out-performs the lateral view angle in terms of differentiating between injury and non-injury cases, and the ability to detect extreme cases.

Acknowledgments

I would like to express my most sincere appreciation to my advisor, Professor Kang Li, for his dedication and encouragement in my study. Prof. Li gives me many interesting projects to think about and work on, from which I have gained precious experiences in both practical and theoretical aspects. Moreover, I truly benefit a lot from the discussion with him, from which I learned most recent research and application trends in the field of image processing and healthcare, and also status quo and future development blueprint of the healthcare industry.

I would also like to thank Prof. Weihong Guo, for teaching the simulation course. Prof. Guo prepares the course material in a very detailed and innovative way, and its almost addictive to listen to her lecture. The knowledge I learned from her course benefit me a lot either in research or in interviews.

I also want to thank Professor Zhimin Xi for being my committee member and offering precious advices.

Most of all, I would like to thank my Mom and Dad. They raised me up with their uttermost care, love and hard work. They give me unconditional support for studying abroad, and sacrifice the time that could have been spent with me. I want to thank my loving and supportive wife who accompanies me with my graduate study.

Dedication

To my wife and my parents.

Table of Contents

List of Tables

List of Figures

Chapter 1

Introduction and Preliminaries

1.1 Introduction

Ulnar-sided dislocation of the carpometacarpal (CMC) joints is an uncommon injury with an incidence around 1% of hand-specific trauma (Eichhorn-Sens, Katzer, Meenen, & Rueger, 2001). This injury usually refers to the dislocations of the fourth or fifth metacarpal from its articulation with the hamate. Since the findings on physical and radiographic examination are subtle, these injuries can be difficult to diagnose at the time of injury with a high rate of missed diagnosis (Lawlis & Gunther, 1991; Pullen, Richardson, McCullough, & Jarvis, 1995). The consequence of missed or delayed diagnosis could be severe. It may lead to long-term pain, arthritis, and decreased grip strength (Fisher, Rogers, & Hendrix, 1983; Hsu & Curtis, 1970; Pullen et al., 1995; Smith, Yang, & Weiland, 1996). The delayed diagnoses may even require an open surgical procedure to prevent late complications (Prokopis & Weiland, 2008; Gunther, 1984).

Diagnosing ulnar-sided dislocation of the carpometacarpal joints traditionally rely on visual inspection of the metacarpal bones on posteroanterior and lateral plain radiographs. A few radiographic screening tools have been developed to aid the diagnosis of carpometacarpal injury. Fisher (Fisher et al., 1983) developed a method based on the parallel M-shape lines (M-lines) on postero-anterior radiographs. The joint dislocation was determined by a break in parallelism of the two M-lines. Since one of the M-lines is along the base of metacarpals 2 to 4 and the other is along the distal ends of the wrist bones including trapezoid, capitate, and hamate, it may be difficult to identify the two lines since they may be obscured by overlap of the hamate. McDonald (McDonald, Shupe, Hammel, & Kroonen, 2011) proposed a method to diagnose the CMC joint dislocation by comparing the angle between the fifth finger metacarpals and the index metacarpal (index-small intermetacarpal angle).

The accuracy of this method could be dependent on the overlap of individual metacarpals on the lateral hand radiograph. It is not easy to obtain a good lateral radiograph without significant overlap of the digits and phalanges in the acute setting due to the varying rotation, pronation, or supination of the hand. These shortcomings have limited the diagnosis effectiveness of the existing methods and may contribute to the missed or delayed diagnosis of ulnar-sided dislocation of the carpometacarpal joints. There is a need to develop more reliable screening measures to improve diagnostic accuracy (Wade, Youngberg, & Liss, 1995). CT scan would not be a feasible screening tool due to increased time, cost and radiation exposure.

The capitate bone has been considered as an easily identified landmark on lateral radiographs, even when multiple metacarpals are affected since the distal carpal row have little overlap with the metacarpal bones. Therefore the capitate bone can be used as the stable biomarker of the distal carpal row. It would be possible for both experienced clinicians and resident-level orthopedic or radiology trainees to utilize the capitate bone for screening carpometacarpal dislocation and fracture-dislocation.

The present study proposed a rigorous computational framework to calculate the 2D intersection angles between ulnar-side metacarpal bones and the capitate bone and examined if the 2D capitate-based intersection angles can better characterize ulnar-sided carpometacarpal joint dislocation.

1.2 Thesis Outline

Chapter two is the main chapter that describes our computational framework step by step, which calculates the intersecting angle of two bones. The computational framework consists of four steps in implementation, where each step utilizes a particular method that is well defined. We describe theoretical backgrounds and implementation details for each step. We will first propose the 2D version of the computational framework, which handles radiographic images; and then propose its counterpart in 3D version that handles CT scans images. We conclude this chapter by showing the framework has controllable error in defining angles.

Chapter three considers the 2D angle from lateral view radiographic images in diagnosing CMC fracture and dislocation. We consider the problem of a classifying injury/non-injury cases, based on the output angles of our computational framework. We show that the proposed angle can reduce the confusion associated with carpometacarpal injuries and has better sensitivity and specificity in comparison to the traditional methods. We encourage readers to find further details in our published paper (Potini, Wu, Li, & Tan, 2017).

Chapter four considers the surrogate angle of the true 3D angle. We first study how well the surrogate angle approximates the true one, and then show its performance in the injury/non-injury classification problem. Notably, by using the surrogate spatial angle, our method achieve the best classification performance.

We conclude the thesis in chapter five with discussion.

Chapter 2

Computational Framework

We propose the angle between capitate and $4^{\text{th}}/5^{\text{th}}$ metacarpal as the diagnosing angle for CMC fracture and dislocation. We consider this angle in (1): lateral view radiograph image, and (2): a surrogate angle for the true 3-D spatial angle, which is constructed from lateral view and postero-anterior (PA) view image. To calculate this angle, we design a semi-automatic computational framework, which is the main purpose of this thesis study. The comptational framework consists of subroutines that are strictly-defined, highlt reproducible, and has minimum inter- and intra- observer variability. We introduce the frameworks for calculating bone intersecting angles on lateral view and PA view, followed by the frameworks for calculating 3D spatial angle.

2.1 2D Angle Calculation

The proposed computational framework is designed to identify the directions of metacarpal and capitate bones, and thus calculate their intersecting angles. It reads hand X-ray images as input and outputs intersection angles of interest including capitate-based angles (the capitate-5th-metacarpal angle and capitate-4th-metacarpal angle) and index-based intersection angles (the index-small intermetacarpal angle). Each step utilizes a well defined method to minimize or even eliminate inter- and intra- observer variability in implementation. The framework consists of following four steps:

The computational framework first extracts the bony contours using a semi-automated algorithm; and then identifies the articulating portions on proximal and distal ends of bones; and finally fits circles onto them. The direction of a bone is defined by linking the circle centers on two ends of this bone. The proposed computational framework is able to

1. Extract bony contours of the 4th/5th and 2nd metacarpal bones, as well as the capitate bone. (Utilizing Algorithm 1 2.1)

2. Calculate the curvature along each bony contour, and identify two articulating portions based on the curvature. (Utilizing Algorithm 2 2.1)

3. Fit circles onto articulating portions, and thus define bones direction. (Utilizing Algorithm 3 2.1)

4. Calculate intersecting angles of two bones.

The four steps are also demonstrated in Figure 2.1. Three different algorithms are used in step 1 to 3, as described in detail in the following. The framework can be applied to both lateral and anterior-posterior (AP) view. A similar framework which takes CT images as inputs and outputs 3D intersecting angles is also proposed.

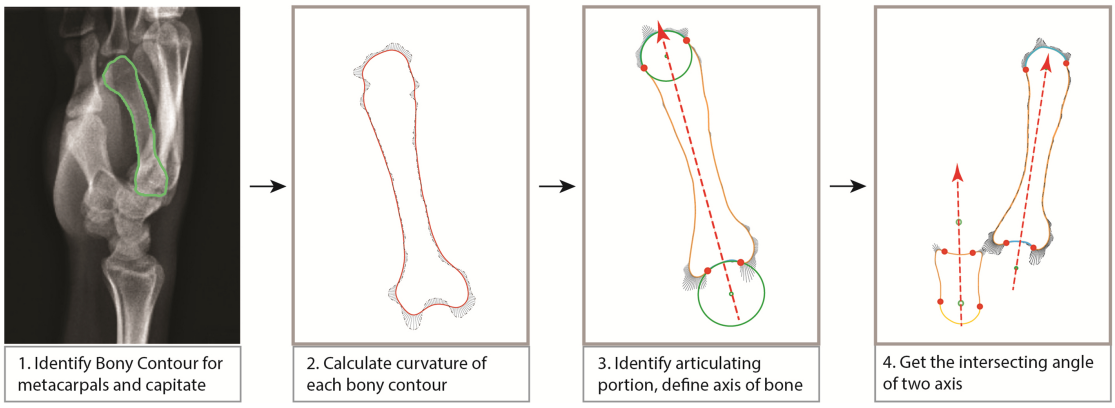

Figure 2.1: Illustration of our computational framework. Steps 1 utilizes Livewire interactive segmentation algorithm to do bony contour extraction. Step 2 identifies articulating portion based on curvature. Step 3 uses least square fitting to fit circles and define bone direction.

Algorithm 1: Bony Contour Identification

The bony contour is identified using an interactive and semi-automated image segmentation technique called Livewire (Barrett & Mortensen, 1997), which allows users to extract the full contour of an object reliably by sequentially selecting a few key points along objects

outline. The method first creates a cost graph of the original image, and then sequentially finds the lowest cost path between two ordered points and thus completes a full contour.

Figure 2.2: Implementation of Livewire method on a lateral view radiograph. Above are four snapshots collected sequentially during contour extraction. Green curve is the contour that the user extracted up to the time the snapshot is took.

The cost graph is built upon the gradient of an image. Suppose we represent an image by f, where $f(i,j)$ is the intensity function at pixel (i,j). Then the gradient at each pixel is a 2D vector consisting of its derivative in horizontal and vertical direction.

$$\nabla f = [g_x, g_y] = \left[\frac{\partial f}{\partial x}, \frac{\partial f}{\partial y}\right] \tag{2.1}$$

The derivative can be approximated by finite difference. The magnitude and direction of the derivative are:

$$|\nabla f| = \sqrt{(g_x)^2 + (g_y)^2}, \quad \theta = \tan^{-1}\frac{g_x}{g_y} \tag{2.2}$$

In practice, the gradient graph can be created by applying a gradient filter like Sobel (Sobel & Feldman, 1968). Suppose we represent cost graph as W, the weights of the cost graph, W_x and W_y are given as the inverse of the derivatives g_x and g_y:

$$W_x = \frac{1}{g_x}, \qquad W_y = \frac{1}{g_y} \tag{2.3}$$

The inverse here is to make stronger edge on the image to have lower cost.

The principle of Livewire (Barrett & Mortensen, 1997) is using Dijkstras algorithm to find lowest cost path between two points on the cost graph, for the reason that lowest cost

path on cost graph correspond to edge on original image. The implementation of Livewire (Barrett & Mortensen, 1997) is interactive: the calculated path would be displayed and changed as the mouse moves over different points. The user can choose a satisfied point and continue this process until a full contour is extracted. An example of contours of different bones is given in Figure 2.3.

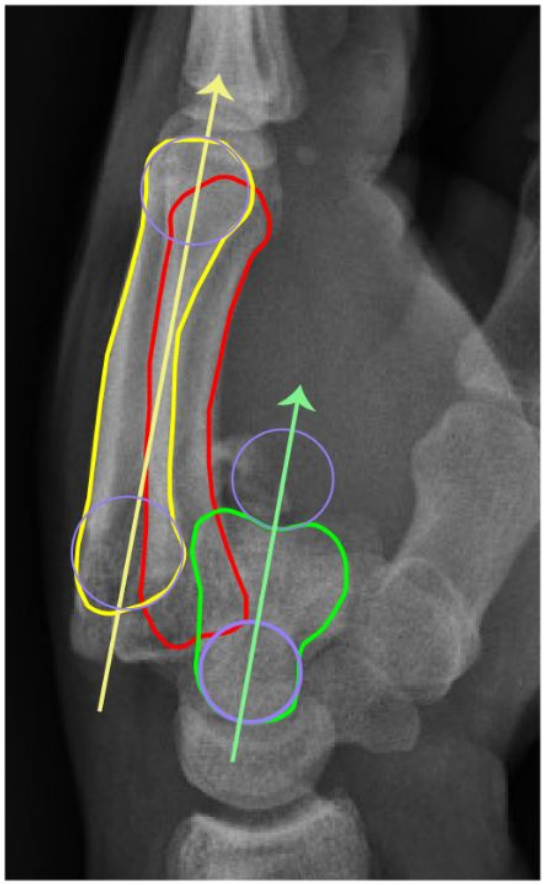

Figure 2.3: Illustration of completed bony contour extraction. Red: 5th metacarpal; Green: 2nd metacarpal; Yellow: capitate.

Algorithm 2: Curvature-based Articulating Surface Identification

This algorithm calculates curvature along the input bony contour, and outputs two articulating portions of a bone, one on proximal end and another on distal end. We explain the theoretical background as follows (Li, S, Fu, Harner, & Zhang, 2010). A sagittal plane bone contour profile $\mathcal{C} = (x, y)$ can be expressed in parametric-form as a function of the arc

length:

$$\mathcal{C}(u) = (x(u), y(u))$$

An evolved version $\mathcal{C}_\sigma$ of $\mathcal{C}$ takes the following form:

$$\mathcal{C}_\sigma = (X(u,\sigma), Y(u,\sigma))$$

where σ is the scale parameter, $X(u,\sigma) = x(u) \otimes g(x,u)$ and $Y(u,\sigma) = y(u) \otimes g(x,u)$,

where $\otimes$ is the convolution operator and $g(x,u)$ denotes a Gaussian of width σ (Marr & Hildreth, 1980). The curvature of $\kappa(u,\sigma)$ is then represented by:

$$\kappa(u,\sigma) = \frac{X_u(u,\sigma)Y_{uu}(u,\sigma) - X_{uu}(u,\sigma)Y_u(u,\sigma)}{(X_u(u,\sigma)^2 + Y_u(u,\sigma)^2)^{\frac{3}{2}}} \tag{2.4}$$

where

$$X_u(u,\sigma) = \frac{\partial}{\partial u}(x(u) \otimes g(u,\sigma)), \qquad X_{uu}(u,\sigma) = \frac{\partial^2}{\partial u^2}(x(u) \otimes g(u,\sigma))$$
$$Y_u(u,\sigma) = \frac{\partial}{\partial u}(y(u) \otimes g(u,\sigma)), \qquad Y_{uu}(u,\sigma) = \frac{\partial^2}{\partial u^2}(y(u) \otimes g(u,\sigma))$$

Figure 2.4: Geometry of distal end of a metacarpal bone. Black short lines: curvature along the bony contour. Two red dots: the points where curvature crosses/touches zero. Blue curve: the corresponding articulating portion enclosed by the two red dots.

The direction and magnitude of curvature are illustrated in Figure 2.4 by the black short lines. The criterion for choosing articulating surface is based on the observation that the articulating and non-articulating surfaces of the bony contour exhibit distinct curvature characteristics (see figure 2.4). There exist two points on each side where curvature crosses or touches zero, distinguishing the articulating and non-articulating surfaces. Thus the articulating portion is defined as the contour between the two curvature zero-crossing points.

Algorithm 3: Circle Fitting on Articulating Surfaces

This algorithm uses least square fitting to fit circles onto the input articulating portions. The reason for fitting circle is based on the observation that the articulating portions of bones are smooth and allow circular motion, and thus can be approximated by circle. For metacarpal bones, circle center is outside the bone for proximal end, and inside the bone for distal end; while for capitate bone its the opposite.

The input for Algorithm 3 is the output of Algorithm 2: articulating portion of a bone profile. It can be denoted by a series of points: (x_i, y_i). Assume the fitted circle radius equals to R, with fitted center locate in (x_c, y_c); then the residual of point (x_i, y_i) is given by:

$$\mathbf{e}_i = \|(x_i, y_i) - (x_c, y_c)\| - R \tag{2.5}$$

Figure 2.5 is a good illustration of their geometric relations.

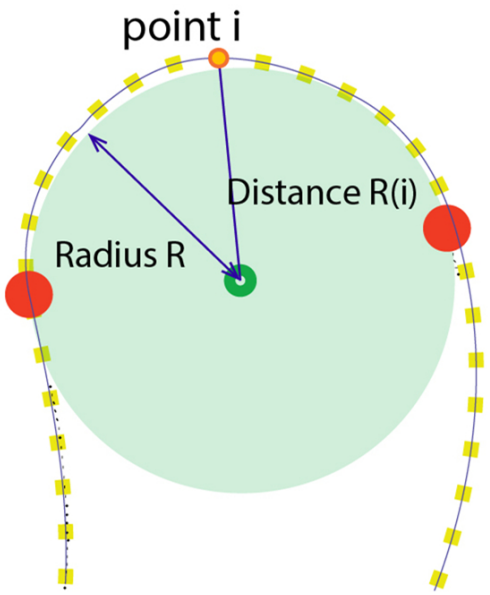

Figure 2.5: Fitting a circle on articulating portion.

The residual sum of squares is given by:

$$RSS = \sum_{i=1}^{n} \mathbf{e}_i^2 = \sum_{i=1}^{n} \left(\sqrt{(x_i - x_c)^2 + (y_i - y_c)^2} - R \right)^2 \tag{2.6}$$

Let $\beta = (x_c, y_c, R)$, The geometric least-square fit algorithm will try to fit this residual sum of squares, that is:

$$\hat{\beta} \equiv \arg\min_{\beta} \sum_{i=1}^{n} \mathbf{e}_i(\beta)^2 \tag{2.7}$$

We used Gauss-Newton method to solve the problem iteratively:

$$\beta \leftarrow \beta - \left(J(\beta)^T J(\beta) \right)^{-1} J(\beta)\mathbf{e}(\beta) \tag{2.8}$$

Where the Jacobian J is defined on the partial derivatives $\frac{\partial \mathbf{e}_i(\beta)}{\partial \beta_j}$:

$$J(\beta) = \begin{bmatrix} \frac{x_c - x_1}{\|(x_c, y_c) - (x_1, y_1)\|} & \frac{y_c - y_1}{\|(x_c, y_c) - (x_1, y_1)\|} & -1 \\ \dots & \dots & \dots \\ \frac{x_c - x_n}{\|(x_c, y_c) - (x_n, y_n)\|} & \frac{y_c - y_n}{\|(x_c, y_c) - (x_n, y_n)\|} & -1 \end{bmatrix} \tag{2.9}$$

We use $\hat{\beta} = (\hat{x}_C, \hat{y}_C, \hat{R})$ to denote the solution in solving the least-square fitting problem.

After getting fitted circles on both ends of a bone, we link the two centroids to define the direction longitudinal axis (direction) of this bone. This process is repeated for each bone, and angle between two bones is defined as the angle between their longitudinal axes.

2.2 3D Angle Calculation

To account for variability on lateral plain radiographs and validate the findings of the 2D angles, the corresponding 3D angles were calculated from CT scans, with similar procedures and criterions as the calculation of 2D angles as follows.

1. Reconstruct 3D models from CT scans, select out the bones that are of interest.
2. Identify articulating surfaces based on curvature.
3. Fit spheres on articulating surfaces of capitate and metacarpal bones.
4. Calculate intersecting angles between bones.

At the first step, we use Mimics (Materialise NV, Leuven, Belgium) software to construct 3D hand model from CT scans DICOM file. An example of a completed 3D hand model is illustrated in Figure 2.6. We select the bones of interest: capitate and 4th/5th metacarpal for our proposed sets of angles; and 2nd metacarpal used for reproducing the method of (McDonald et al., 2011). On Figure 2.6, the capitate bone is marked in yellow, 4th/5th metacarpal bones are marked in pink/green, and the 2nd metacarpal is marked in light lake blue.

Figure 2.6: Reconstruction of 3D bone models.

At the next step, the curvature of each selected bone will be calculated. This process can be done automatically by Geomagic Software (3D Systems, North Carolina, USA). Figure **??** is an example of the calculated curvature on the surface of capiate bone. Colors on the 3D model represent the magnitude of the curvature. The more red the color is, the more positively large the curvature is. On the other hand, the more green the color is, the more negatively large the curvature is. On the distal articulating surface of capitate, we can see there is a nature close loop in yellow color, represents that the curvature is zero.

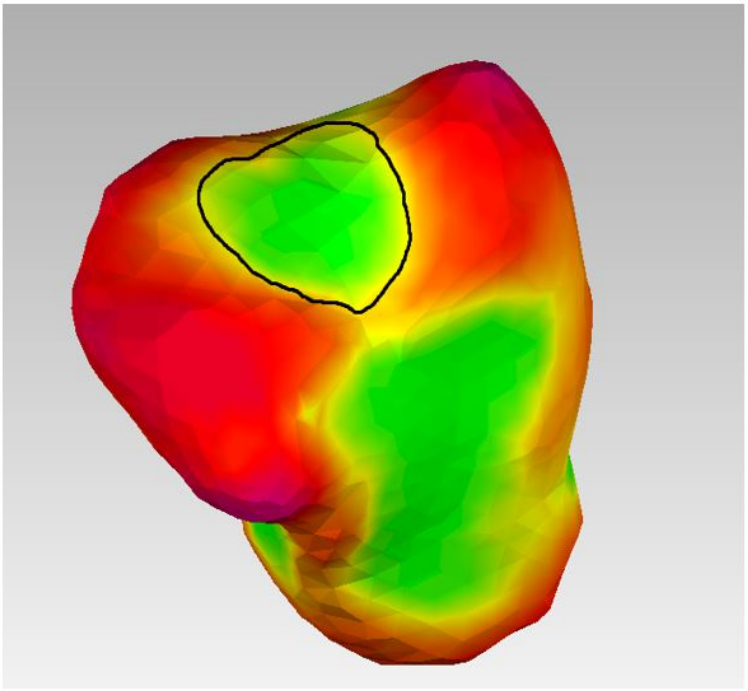

Figure 2.7: Color represents magnitude (positive and negative) of curvature. The black closed loop is the curvature zero-crossing line, and all triangle surfaces inside the loop are used for sphere fitting. B: A sphere is fitted. C: Two spheres are fitted and their center are linked to define the direction of the bone

We choose the region inside this closed loop to fit a sphere, as shown on **??**-Left. We do the same on the other end (proximal end). As shown on Figure **??**-Right, two spheres are fitted on distal and proximal ends of capitate, representing its articulating function.

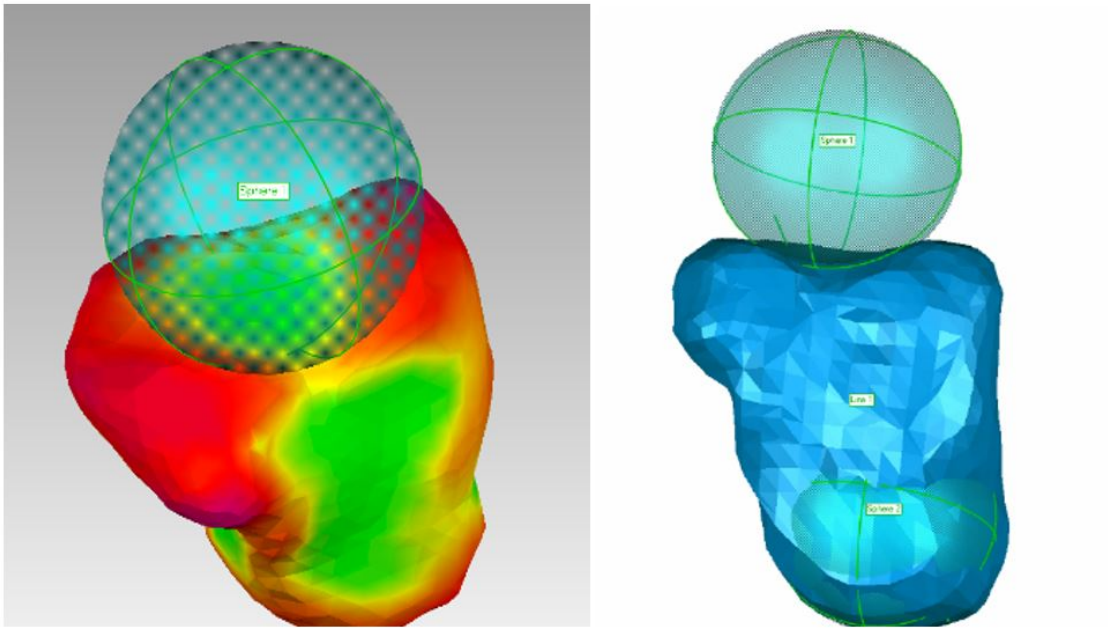

Figure 2.8: Left: A sphere is fitted. Right: Two spheres are fitted and their center are linked to define the direction of the bone

The centroids of spheres is obtained by fitting the surface data by a least-squares geometric fitting algorithm. Given n surface points (n typically ranged from 800 to 1200), the algorithm determined the centroid coordinates (x_c, y_c, z_c) and radius R of the sphere, by minimizing the following residual sum of square:

$$RSS = \sum_{i=1}^{n} \mathbf{e}_i^2 = \sum_{i=1}^{n} \left(\sqrt{(x_i - x_c)^2 + (y_i - y_c)^2 + (z_i - z_c)^2} - R \right)^2 \tag{2.10}$$

Let $\beta = (x_c, y_c, z_c, R)$, the geometric least-square fit algorithm will try to fit this residual sum of squares which is:

$$\hat{\beta} \equiv \arg\min_{\beta} \sum_{i=1}^{n} \mathbf{e}_i(\beta)^2 \tag{2.11}$$

In our study, the 3D model is actually consist of a large amount of tiny 2D surface triangles, and thus the surface point for fitting is chosen as the average of the three vertices of each triangle (which is also the gravity center of it). The fitting process can also be implemented automatically in Geomagic Software.

After getting two spheres on both proximal and distal ends of a bone, the long axis of the bone is defined as the line linking the two centroid of the spheres. The intersecting spatial

angles are defined as the angles between the corresponding long axes and used as the gold standard. Note that in the next chapter we propose a surrogate spatial angle, which is based on 2D angles and is different from the 'true' spatial angle defined here. We will perform a comparative study to evaluate the 2D angles obtained from our proposed computational framework, the surrogate spatial angles constructed based on 2D angles, against the 3D measures defined here.

2.3 Fitting Errors

The proposed computational framework successfully segmented the bony contours, identified articulating surfaces, and fitted the articulating portions with circles. We use percentage-root-mean-square error (PRMSE) to quantify the fitting quality of the fitting step. PRMSE is chosen as a criterion because it is a scale-invariant error measure, regardless of image and bone size.

The quality of fitting, represented by the percentage-root-mean-square-error (PRMSE), are listed in Table 2.1.

$$PRMSE = \frac{\sqrt{\frac{1}{n}\sum_{i=1}^{n}\left(\|X_i - \hat{X}_C\|_2 - \hat{R}\right)^2}}{\hat{R}} \tag{2.12}$$

Where $X_i = (x_i, y_i), \hat{X}_C = (\hat{x}_C, \hat{y}_C)$ in 2D case, and $X_i = (x_i, y_i, z_i), \hat{X}_C = (\hat{x}_C, \hat{y}_C, \hat{z}_C)$ in 3D case.

We show the PRMSE results for metacarpal bones and capitate bone, on 2D lateral view, 2D postero-anterior (PA) view and 3D view. The following results are calculated from our database with 60 cases.

PRMSE	2nd Metacarpal	4th Metacarpal	5th Metacarpal	Capitate
2D - Lateral	5.83%(±3.92%)	5.22%(±3.75%)	5.58%(±4.02%)	4.76%(±2.88%)
2D - AP	4.71%(±2.85%)	4.62%(±2.88%)	4.48%(±2.98%)	3.95%(±2.06%)
3D	3.86%(±1.93%)	3.76%(±1.78%)	3.97%(±2.02%)	3.21%(±1.43%)

Table 2.1: Fitting error of approximating articulating surfaces as circle (2D)/sphere (3D).

The high fitting quality indicated by the low error authenticates the assumption that articulating portion is circle shape, and also confirms that our computational framework has limited error in the fitting step.

Chapter 3

Angle On Lateral View

This chapter is a brief version of our published paper (Potini et al., 2017), we encourage readers to find more details therein. In this chapter we focus on the capitate-$4^{\text{th}}/5^{\text{th}}$ metacarpal angle in differentiating injury/non-injury cases. We consider the general problem of injury/non-injury classification problem and view the above angle as a classifier and study its performance.

This angle is the direct output from our computational framework. It has the ideal property that these angles are larger in the injured hands, which agrees to clinical examinations. We conduct statistical test to demonstrate that the difference of such angles are statistically different between injured and non-injured groups.

3.1 Database

The proposed computational frameworks were empirically tested based on the data acquired from our departmental database of all patients who underwent surgery for ulnar-sided carpometacarpal dislocation from 2003 to 2013 after receiving institutional review board approval. Within this initial operative group, all patients with posteroanterior and lateral radiographs and preoperative computed tomography (CT) scan of the hand or wrist were selected as the study group. The study group has 25 patients with 45 ulnar-sided carpometacarpal dislocations. Of these patients, 20 had injuries to the fourth and fifth carpometacarpal joints on the same hand, 2 had an isolated fourth carpometacarpal dislocation, and 3 had an isolated fifth carpometacarpal dislocation. The control group consisted of 27 patients treated during the same time period who had both CT scan and plain radiographs of the hand and wrist, but without evidence of bony carpal or metacarpal pathology, as determined by an attending radiologist.

The mean (SD) age, body weight, and body height at the time of study were 30.7 ± 11.6 years, 77.3 ± 14.7 kg, and 175.7 ± 9.9 cm, respectively. The CT scans were collected with slice spacing of 1.25 mm, 28 cm field of view and 512×512 pixels per image (0.547 mm/pixel in-plane resolution). The resulting slices were reconstructed into 3D solid models using Mimics, software (Materialise NV, Leuven, Belgium).

3.2 Method Evaluation

The computational framework is applied to calculate the 2D intersection angles, including capitate-based angles (capitate-5th metacarpal and capitate-4th metacarpal angles) and index-based intersection angles (index-small inter-metacarpal angle) (McDonald et al., 2011) for comparison purpose. We calculate angles on both lateral view and PA view radio-graph images.

We investigate whether the intersection angles can characterize the carpometacarpal fracture and dislocation. More specifically, we perform a hypothesis test to check if there exist a statistically significant difference between the study group and the control group, using the capitate-based angle (capitate-5th metacarpal and capitate-4th metacarpal angle), as well as the index-small inter-metacarpal angle. We also show the results using a box-plot.

Finally we assess the inter-observer reliability of both methods calculated by our computational framework. Inter-observer reliability is used to assess the degree to which different users will give consistent estimates from the proposed method. It is indicated by a mean intra-class correlation coefficient (ICC). A high value of ICC means the degree to which individual resembles each other. We output the ICC in table 4.

3.3 Results

For study (injured) group and control (uninjured) group, we give the comparison of our proposed angle: capitate-5th angle and capitate-4th, as well as the index-small inter-metacarpal angle (abbr. IS IMA) proposed by (McDonald et al., 2011). For each angle, we perform a statistical T-test with the null hypothesis: the mean does not differ between injury and non-injury group.

Angle	**Group**	**Mean**	**Standard Deviation**	**Range**	**p-value**
Capitate-4th Lateral	Injured	17.68	6.12	9 ∼ 28	$< .01$
	Non-injured	10.06	4.89	2 ∼ 21	
Capitate-4th AP	Injured	15.56	7.7	1 ∼ 26	0.18
	Non-injured	12.9	5.89	2 ∼ 24	
Capitate-5th Lateral	Injured	18.74	6.95	9 ∼ 29	0.03
	Non-injured	11.78	6.29	2 ∼ 20	
Capitate-5th AP	Injured	16.82	5.59	7 ∼ 25	0.33
	Non-injured	15.6	4.74	5 ∼ 23	
I-S IMA Lateral	Injured	12.18	6.63	4 ∼ 23	0.11
	Non-injured	8.27	5.99	0 ∼ 25	
I-S IMA AP	Injured	23.86	4.9	15 ∼ 31	0.21
	Non-injured	23.1	4.31	12 ∼ 30	

Table 3.1: Comparison of 2-D angles.

From the above table, we can clearly observe that for capitate-4th and capitate-5th angles on lateral view, there exist statistically significant difference between injured and non-injured groups. However for other angles, we don't have enough evidence to make such statements.

We also show the box-plots of the three angles between injured/non-injured groups, on lateral view and PA view respectively.

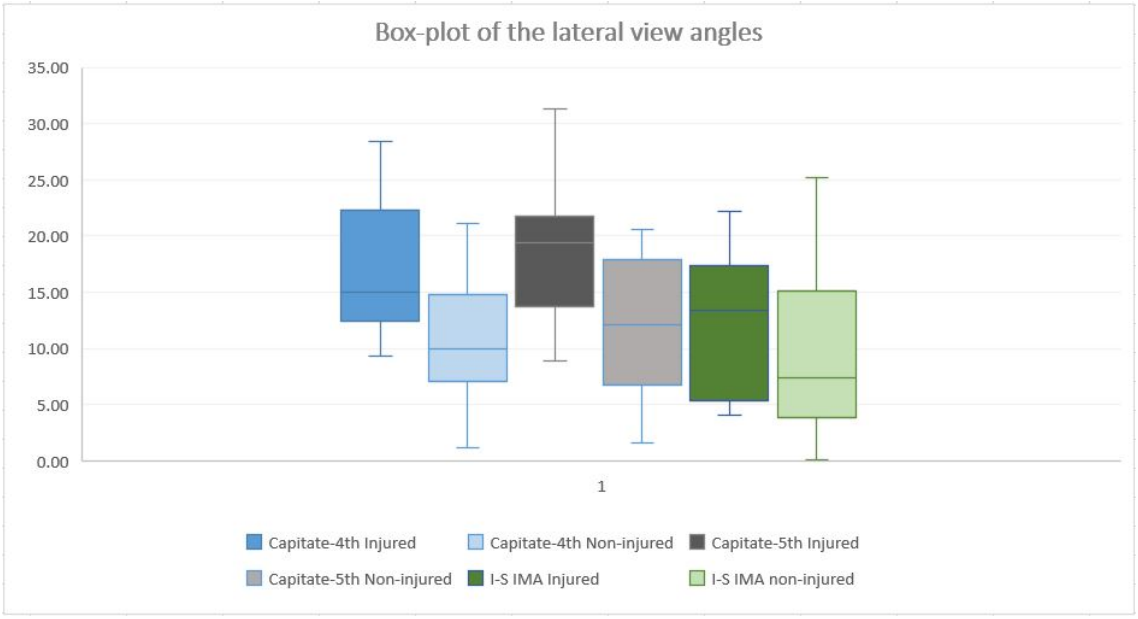

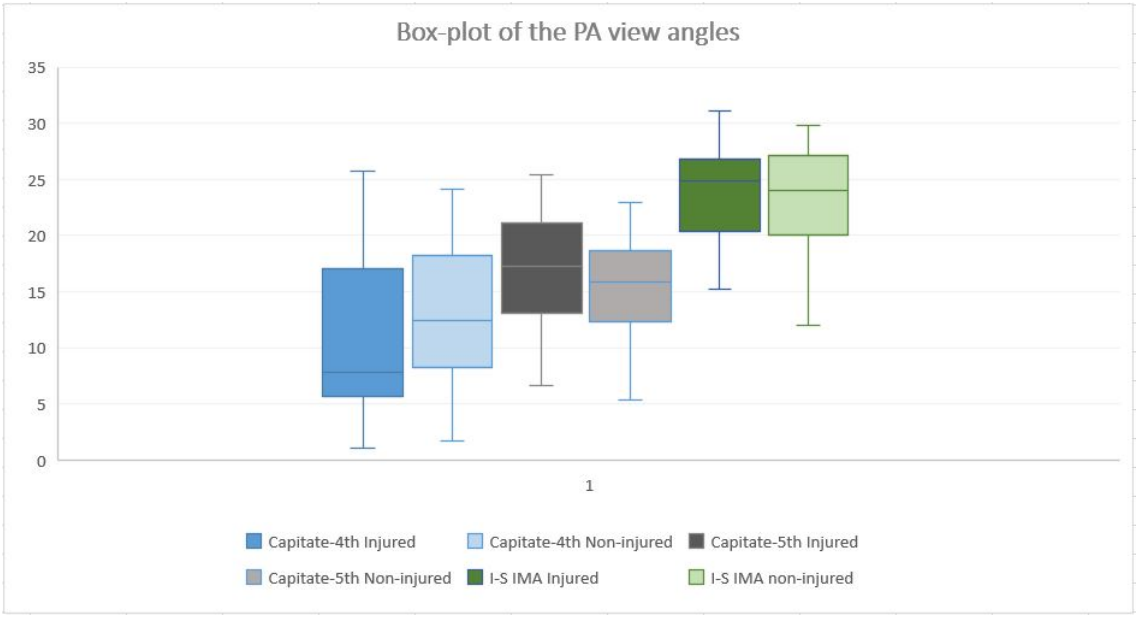

From the above box-plots we can draw the same conclusion that lateral view capitate-4th and capitate-5th angles are able to differentiate between injured and non-injured groups.

Finally, we evaluate the inter-observer reliability by mean intra-class correlation coefficient (abbr. ICC), as shown on the table below:

Angle	ICC
Capitate-4th	0.95
Capitate-5th	0.95
I-S IMA	0.93

Table 3.2: ICC for different angles

Chapter 4

Surrogate 3D Angle

In this chapter we focus on the surrogate 3D angle between capitate and $4^{\text{th}}/5^{\text{th}}$ metacarpal. The surrogate angle is calculated from 2D angles in lateral and PA view:

$$\hat{\theta} = \sqrt{\theta^2_{\text{lateral}} + \theta^2_{\text{PA}}} \tag{4.1}$$

4.1 Method Evaluation

We use the lateral view angles and PA view angles calculated from last chapter, and construct the surrogate 3D angle using equation 4.1. The true 3D angle is also calculated from the 3D version of our computational framework.

We first evaluate how accurate the surrogate angle approximates the true 3D angle, by plotting their relation.

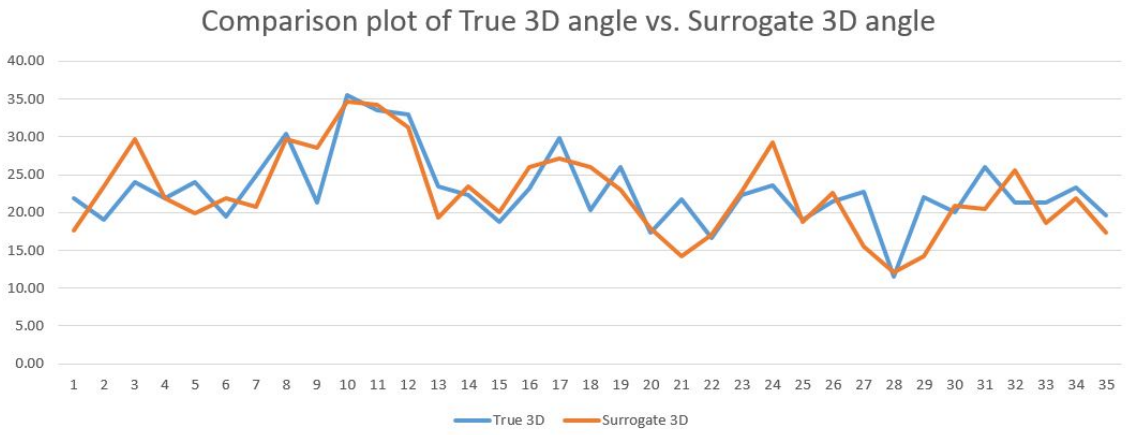

Figure 4.1: The above plot shows the difference between true 3D and surrogate angle of the capitate-5th metacarpal angle. x-axis is case number, and y-axis is the absolute value of the angle.

We skip the plots for capitate-4th and I-S IMA, which shows similar patterns as above. We can see that the surrogate angle is a very good approximation to the true 3D angle.

We then show the percentage absolute error (PAE) of using surrogate angle to approximate true 3D anlge.

Angle	Capitate-4th	Capitate-5th	I-S IMA
PAE	0.16	0.12	0.12

Table 4.1: Percentage absolute error (PAE) of using surrogate 3D angle to approximate true 3D angle.

Then we investigate whether the surrogate angles can characterize the carpometacarpal fracture and dislocation. More specifically, we perform a hypothesis test to check if there exist a statistically significant difference between the study group and the control group, using the capitate-based angle (capitate-5th metacarpal and capitate-4th metacarpal angle), as well as the index-small inter-metacarpal angle. We also show the results using a box-plot.

4.2 Results

For study (injured) group and control (uninjured) group, we give the comparison of our proposed angle: capitate-5th angle and capitate-4th, as well as the index-small inter-metacarpal angle (abbr. I-S IMA) proposed by (McDonald et al., 2011). For each angle, we perform a statistical T-test with the null hypothesis: the mean does not differ between injury and non-injury group.

Angle	Group	Mean	Standard Deviation	Range	p-value
Capitate-4th	Injured	22.42	4.35	17 ∼ 32	.02
	Non-injured	17.42	4.56	6 ∼ 24	
Capitate-5th	Injured	26.14	4.68	21 ∼34	0.01
	Non-injured	20.5	4.58	12 ∼ 27	
I-S IMA	Injured	27.56	3.98	24 ∼ 35	0.13
	Non-injured	25.75	5.83	6 ∼ 33	

Table 4.2: Comparison of surrogate 3D angles.

From the above table, we can clearly observe that for the capitate-4th and capitate-5th angles, there exist statistically significant difference between injured and non-injured groups. However for the I-S IMA angle, we don't have enough evidence to make such statement.

We also show the box-plots of the three angles between injured/non-injured groups.

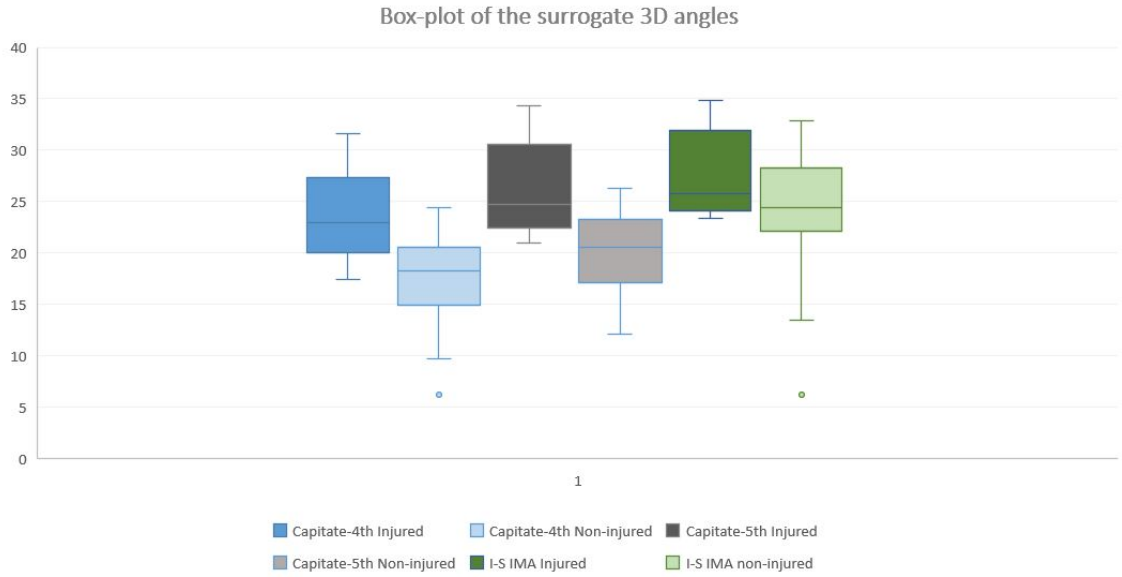

Figure 4.2: Box-plot of the surrogate 3D angles of the capitate-4th/5th angle and the index-small inter-metacarpal angle.

We can see from box-plot that fro capitate-based 3D surrogate angles, there exist a significant difference between the injured and non-injured group.

4.3 Advantage Of Using 3D Surrogate Angle

Compared with the box-plot of 2D capitate-based angles on lateral view, the distributions of injured group and non-injured group from 3D surrogate angles are more separated, and thus it's easier to differentiate between two groups.

Another reason why the surrogate angle performs better than the lateral counterpart is that it can sometimes identify potential dislocation which cannot be seen when using 2D angles. Below we show an example of a same injured joint. This patient undergoes a severe hand injury, all metacarpals are dislocated. In such case, the angle between index finger and small finger will remain usual, and on 2D view even the angle between metacarpal and capitate is usual. Only the 3D angles show anomaly. The capitate-5th angle on 2D lateral view is 5, the same angle on 3D view is 22, and the surrogate angle is 20.

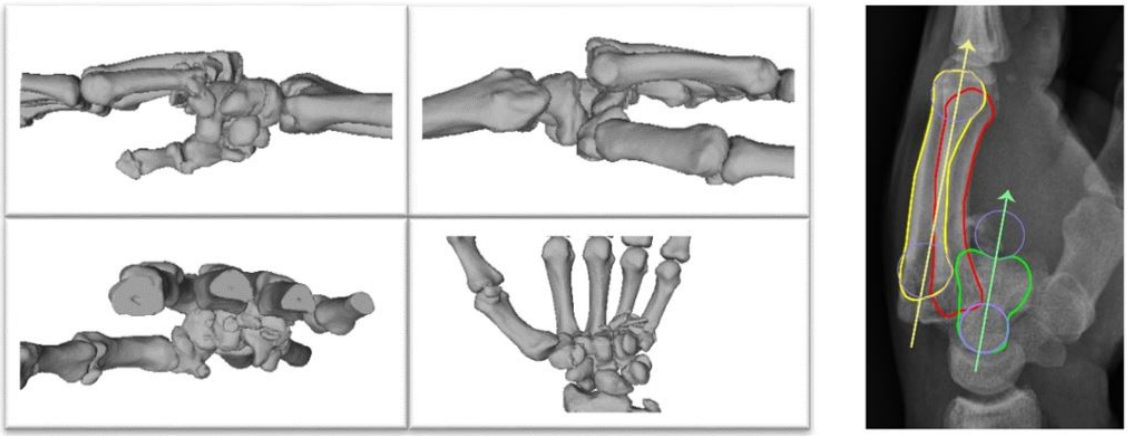

Figure 4.3: A case showing that 2D angles not being able to diagnose CMC fracture and dislocation, but 3D angles being able to.

Yet another practical reason is that patients don't have to be exposed to excessive CT radiations, only two X-ray images, yet its' possible to get a close enough measure of the true 3D angle.

Chapter 5

Discussion

We have proposed a computational framework to calculate the capitate-based angles for characterizing carpometacarpal dislocation and fracture-dislocation based on the observation that the capitate is relatively easy to identify on lateral radiographs. Carpometacarpal dislocation is often hard to diagnose in initial physical exam due to the lack of obvious clinical signs of joint dislocation and considerable amount of swelling accompanied. More than 60% of this type of injuries may be missed on initial assessment as reported in the retrospective studies. (Lawlis & Gunther, 1991; Pullen et al., 1995) Previous studies have examined medical radiographs on the oblique or poster-anterior view for diagnosing the CMC dislocation. These radiographs may not be effective in diagnosis due to heavy overlapping of bones. When the CMC dislocation is suspected, oblique radiographs at 30° to 45° injury have been recommended to use for diagnosis (Bora & Didizian, 1974; Cain, Shepler, & Wilson, 1987). Fisher (Fisher et al., 1983) proposed a diagnosing method to identify the parallel M-lines that follow the contour of the distal carpal row along the trapezoid, capitate, and hamate in poster-anterior radiographs to check for joint symmetry. This method may not work well since the typical carpometacarpal dislocation is in the direction parallel to the plane of a posteroanterior radiograph (Yoshida et al., 2003). A recent method (McDonald et al., 2011) characterized carpometacarpal fracture-dislocation from lateral radiographs using an index-based intersection angle between the small finger metacarpal and the index metacarpal (I-S IMA). This method showed better sensitivity and specificity than the methods developed in 70s-80s (Bora & Didizian, 1974; Cain et al., 1987; Fisher et al., 1983). However, this method may function poorly since it is often difficult to identify metacarpal bones and the index-based intersection angle may also be affected by the hand position (Koh, Lee, Lim, Seo, & Park, 2013). Our analysis has shown that using capitate-based angles can result in

the statistical significance for both clinical lateral radiographs and true lateral 3-dimensional reconstruction while the index-based angles used in the previously mentioned methods11 may fail to detect the statistical significance. This suggests that capitate-based angles can better characterize carpometacarpal dislocation.

The proposed computational framework provides a reliable and accurate way to calculate the capitate-based angles. The previously mentioned methods (Fisher et al., 1983; McDonald et al., 2011) require physicians to manually determine contours or direction of a bone, either under PA view or lateral view. These manual process could suffer from errors considering the heavy overlap on lateral view images; or at least introduce inter- and intra-observer variability. This framework has the advantages of high accuracy and low inter- and intra- observer variability. It combines the power of computational image analysis with expert knowledge to extract accurate contours of capitate and metacarpal bones using an interactive contour segmentation method and then using well-defined mathematical definitions to calculate the intersection angles. This interactive contour segmentation method uses Livewire (Barrett & Mortensen, 1997) to automatically calculate edge between any two points and extract contour of a bone and thus minimize human interventions. Another reason we choose the interactive contour segmentation method is due to the intricate nature of our images. On the posteroanterior view radiographs, the carpometacarpal joints are obstructed by overlap of the hamate; on the lateral radiographs, as we also observed, the metacarpals are heavily overlapped (Koh et al., 2013). Fully automated segmentation methods may produce non-uniform or nonsensical contour because of the intricacy in lateral view image and lack of expert participation. Thus the interactive approach, which makes use of both computer graphical analysis and human expertise, works best among the three types of segmentation in our case. Such a procedure is not only more effortless but also highly consistent. Therefore, the definition of a bone no longer solely relies on a physicians visual discretion, but is based on a well-defined consistent criterion. Considering the geometric least square fitting gives a unique circle, the direction of bone is fixed once the contour is extracted. Thus our computing framework is built based on a series of well-defined criteria and thus has minimum inter- and intra- observer variability, which is validated by our testing results.

The present work has shown that the capitate-metacarpal angle can be used as a screening tool for carpometacarpal injury. When the angle is greater than 15°, a carpometacarpal injury very likely and further work-up is needed such as a CT scan. The proposed framework can obtain the capitate-metacarpal angle accurately and reliably and should be considered to integrate into computer-aided diagnostic systems to help clinicians to evaluate patients with inconclusive findings on physical examination, dorsal hand swelling, and ulnar-sided hand pain.

The current work is limited to the CMC joints and metacarpals. The concepts underlying the proposed framework including pattern recognition to segment the bony profile, extracting articulating center based on curvature, and parametric least-squares fitting, can be extended to analysis of other bone injury analysis.

References

Barrett, W. A., & Mortensen, A., William. (1997). Interactive live-wire boundary extraction. *Medical Image Analysis*, *1*(4), 331-341.

Bora, F. J., & Didizian, M. (1974). The treatment of injuries to the carpometacarpal joint of the little finger. *J Bone Joint Surg Am*, *56*(7), 1459-1463.

Cain, J. J., Shepler, T., & Wilson, M. (1987). Hamatometacarpal fracture-dislocation: classification and treatment. *Hand Surg Am*, *12*(5.2), 762-767.

Eichhorn-Sens, J., Katzer, A., Meenen, N., & Rueger, J. (2001). Carpometacarpal dislocation injuries [in german]. *Handchir Mikrochir Plast Chir.*, *33*(3), 189.

Fisher, M., Rogers, L., & Hendrix, R. (1983). Systematic approach to identifying fourth and fifth carpometacarpal joint dislocations. *AJR Am J Roentgenol.*, *140*(2), 319-324.

Gunther, S. (1984). The carpometacarpal joints. *Orthop Clin North Am*, *15*(2), 259-277.

Hsu, J. D., & Curtis, R. M. (1970). Carpometacarpal dislocations on the ulnar side of the hand. *J Bone Joint Surg Am*, *52*(5), 927-930.

Koh, K., Lee, H., Lim, K., Seo, J., & Park, M. (2013). Effect of wrist position on the measurement of carpal indices on the lateral radiograph. *J Hand Surg Eur*, *38*(5), 530-541.

Lawlis, J., & Gunther, S. (1991). Carpometacarpal dislocations: long-term follow-up. *J Bone Joint Surg Am*, *73*(1), 52-59.

Li, K., S, T., Fu, F., Harner, C., & Zhang, X. (2010). Automating analyses of the distal femur articular geometry based on three-dimensional surface data. *Annals of biomedical engineering*, *38*, 2928-2936.

Marr, D., & Hildreth, E. (1980). Theory of edge detection. *Proc. R. Soc. Lond.*, *207*(B), 187-217.

McDonald, L., Shupe, P., Hammel, N., & Kroonen, L. (2011). The intermetacarpal angle screening test for ulnar-sided carpometacarpal fracture-dislocations. *J Hand Surg Am*,

37(9), 1839-1844.

Potini, V. C., Wu, K., Li, K., & Tan, V. (2017). A novel screening technique for carpometacarpal dislocations. *Orthopedics*, *40*(2), 352-356.

Prokopis, P. M., & Weiland, A. J. (2008). Volar dislocation of the fourth and fifth carpometacarpal joints: a case report and review of the literature. *HSS J.*, *4*(2), 138-142.

Pullen, C., Richardson, M., McCullough, K., & Jarvis, R. (1995). Injuries to the ulnar carpometacarpal region: are they being underdiagnosed? *Aust N Z J Surg*, *65*(4), 257-261.

Smith, G., Yang, S., & Weiland, A. (1996). Multiple carpometacarpal dislocations. a case report and review of treatment. *Am J Orthop (Belle Mead NJ)*, *25*(7), 502-506.

Sobel, I., & Feldman, G. (1968). A 3x3 isotropic gradient operator for image processing. *Presentation at Stanford A.I. Project.*.

Wade, J., Youngberg, R., & Liss, R. (1995). Reducing duplicate hand and wrist series in the emergency room: experience at madigan army medical center. *Mil Med*, *160*(1), 37-38.

Yoshida, R., Shah, M., Patterson, R., Buford, W. J., Knighten, J., & Viegas, S. (2003). Anatomy and pathomechanics of ring and small finger carpometacarpal joint injuries. *J Hand Surg Am*, *28*(6), 1035-1043.